

Article

# Effect of the Process Parameters on the Energy Transfer during the Synthesis of the $2\text{LiBH}_4\text{-MgH}_2$ Reactive Hydride Composite for Hydrogen Storage

Julian Jepsen <sup>1,2</sup>, Giovanni Capurso <sup>1,\*</sup>, Julián Puszkiel <sup>1,3</sup>, Nina Busch <sup>1</sup>, Tobias Werner <sup>1</sup>, Chiara Milanese <sup>4</sup>, Alessandro Girella <sup>4</sup>, José Bellosta von Colbe <sup>1</sup>, Martin Dornheim <sup>1</sup> and Thomas Klassen <sup>1,2</sup>

<sup>1</sup> Institute of Materials Research, Helmholtz-Zentrum Geesthacht, 21502 Geesthacht, Germany; julian.jepsen@hzg.de (J.J.); julian.puszkiel@hzg.de (J.P.); nina.busch.hzg@gmx.de (N.B.); tobias.werner.hzg@gmx.de (T.W.); jose.bellostavoncolbe@hzg.de (J.B.v.C.); martin.dornheim@hzg.de (M.D.); klassen@hsu-hh.de (T.K.)

<sup>2</sup> Institute of Materials Technology, Helmut Schmidt University, 22043 Hamburg, Germany

<sup>3</sup> Department of Physicochemistry of Materials, Consejo Nacional de Investigaciones Científicas y Técnicas (CONICET), Centro Atómico Bariloche, R8402AGP S.C. de Bariloche, Argentina

<sup>4</sup> Pavia H2 Lab, Department of Chemistry, Physical Chemistry Division, University of Pavia, 27100 Pavia, Italy; chiara.milanese@unipv.it (C.M.); buondi.giro@gmail.com (A.G.)

\* Correspondence: giovanni.capurso@hzg.de; Tel.: +49-4152-87-2565; Fax: +49-4152-87-2625

Received: 22 February 2019; Accepted: 16 March 2019; Published: 19 March 2019



**Abstract:** Several different milling parameters (additive content, rotation velocity, ball-to-powder ratio, degree of filling, and time) affect the hydrogen absorption and desorption properties of a reactive hydride composite (RHC). In this paper, these effects were thoroughly tested and analyzed. The milling process investigated in such detail was performed on the  $2\text{LiH-MgB}_2$  system doped with  $\text{TiCl}_3$ . Applying an upgraded empirical model, the transfer of energy to the material during the milling process was determined. In this way, it is possible to compare the obtained experimental results with those from processes at different scales. In addition, the different milling parameters were evaluated independently according to their individual effect on the transferred energy. Their influence on the reaction kinetics and hydrogen capacity was discussed and the results were correlated to characteristics like particle and crystallite size, specific surface area, presence of nucleation sites and contaminants. Finally, an optimal value for the transferred energy was determined, above which the powder characteristics do not change and therefore the RHC system properties do not further improve.

**Keywords:** hydrogen storage;  $\text{LiBH}_4/\text{MgH}_2$ ; metal hydrides; borohydrides; reactive hydride composites; high-energy milling

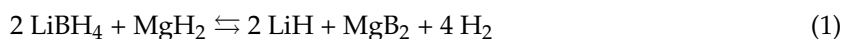
## 1. Introduction

Starting from production using renewable sources, to storage using physical or chemical methods, along with the transformation into energy by means of several kind of fuel cells (FCs), hydrogen technologies have been considered for decades as the most promising energy carrier for the future [1–3]. The issue of hydrogen storage requires therefore a special attention, because the hydrogen molecules offer already in standard conditions a large energy density per unit mass of  $33.33 \text{ kWh kg}^{-1}$  [1,2]. In contrast, due to its low density, the gas has a very low energy density per unit volume in these conditions ( $2.99 \text{ kWh m}^{-3}$ ) [4]. The energy density per unit volume has to be increased without impairing the value of gravimetric density too much, to be in line with several other energy

storage technologies like Li-ion batteries ( $\sim 0.2 \text{ kWh kg}^{-1}/\sim 500 \text{ kWh m}^{-3}$ ), compressed natural gas ( $\sim 13.9 \text{ kWh kg}^{-1}/\sim 2700 \text{ kWh m}^{-3}$ ), or even gasoline ( $\sim 12.2 \text{ kWh kg}^{-1}/\sim 8700 \text{ kWh m}^{-3}$ ) [5]. The storage method allows increasing this value significantly. Considering physical storage, hydrogen can be either compressed at 700 bar or liquefied at cryogenic temperatures (20 K). These physical methods are conceptually straightforward and hence attractive. However, the pressurized gas vessel presents key issues in the material, design and sealing; in addition, reaching the desired pressure requires more than 10% of the stored energy [6,7]. In the cryogenic method, large amounts of energy are also required for liquefaction and boil-off losses. Therefore, both these methods are energy demanding and not the most indicated ones from an economical perspective [7,8]. The highest value of energy per unit volume can be reached placing the hydrogen atoms inside the crystal lattice of a compound, for example a metal; in this manner, hydrogen forms a metal hydride with the host metal. In general, all the hydrides benefit from the lack of intermolecular repulsive forces of the  $\text{H}_2$  molecules owing to the chemical bonds formed with the host atoms. This reaction and, by extension, a reactor system containing the material, are relatively uncomplicated and could be operated just by the application of a moderate hydrogen pressure. A hydrogen pressure higher than a threshold leads to absorption, a loading process, whereas a pressure lower than that leads to desorption, or unloading.

Hydrides, generated from metals such as magnesium hydride ( $\text{MgH}_2$ ) [9,10], or in more complex structures [11] such as tetrahydroborates (e.g.,  $\text{LiBH}_4$ ) [12], alanates [13], and amides [14], have been investigated for many years for hydrogen storage. However, their applicative use has always been hindered by slow reaction kinetics, mainly due to the high activation energy values of the reactions. The activation energies are controlled by mechanisms such as slow diffusion processes, inadequate nucleation and infrequent dissociation of the  $\text{H}_2$  molecule on the material-gas interface, among others. Considerable advances were made through the application of different approaches and the combination of them: inclusion of several additives with catalytic effect [15–17], the use of proper processing techniques [18–20] and the application of nanosupports [21–23].

Owing to some of the aforementioned assets, such as a hydrogen storage gravimetric capacity of 7.6 wt.%, magnesium hydride is considered among the most promising materials for hydrogen storage. Nevertheless, its high thermodynamic stability restricts the practical use of the  $\text{Mg}/\text{MgH}_2$  system [24,25]. In order to decrease the enthalpy value, the concept of Reactive Hydride Composites (RHCs) was proposed. This concept is about the combination of  $\text{MgH}_2$  with low-weight complex hydrides [26,27]. The complex hydride lithium borohydride ( $\text{LiBH}_4$ ) is hereby of special interest, being among the compounds with the highest theoretical hydrogen gravimetric capacity (18.5 wt.% [28]). The combination of  $\text{MgH}_2$  with  $\text{LiBH}_4$ , commonly known as Li-RHC, reduces the theoretical thermodynamic stability, lowering the enthalpy to the theoretical value of  $46 \text{ kJ mol}^{-1} \text{ H}_2$ , according to the reaction in Equation (1) and the corresponding enthalpies of formation [4]:



Including titanium trichloride ( $\text{TiCl}_3$ ) as an additive and ball milling the mixture in a high-energy planetary mill, the reaction kinetics was improved [16]. In previous works, the basic thermodynamic and kinetic characteristics of the  $\text{TiCl}_3$ -doped Li-RHC were thoroughly studied [29,30]. Nonetheless, there are on-going investigations about the effect of both the additive and the milling process [31–33].

The milling process provides a refined microstructure of reactants: reduced particle and crystallite sizes [34], which increase the reaction rate of hydrogen with the host material, mostly due to a greater specific surface and a higher number of paths of diffusion through the crystallite and phase boundaries [35]. It is hypothesized that the particles and crystallites sizes, and consequently the kinetic characteristics, depend on the transfer of energy to the powder material by milling.

In this paper, the effects of the additive are examined to a greater extent and the connection to the additive amount and the energy embedded with milling is discussed. The content of the  $\text{TiCl}_3$  additive is studied in the range between 0 and 0.05 mol. To comprehend better the connection between several milling parameters and the energy transferred with grinding, a comprehensive examination of this

phenomenon has been performed and a revised energy transfer model was adopted [36]. The milling parameters here considered are: (a) milling time; (b) ball-to-powder ratio (BPR); (c) milling velocity, expressed in revolutions per minute (rpm); (d) degree of filling of the vial (percentage of filling). The expression “rotation velocity”, is also frequently used in the scientific literature and is conveyed here by means of “milling velocity”. It defines the velocity of the supporting ground plate inside the planetary mill. The impact of the different BPR at different milling times was also analyzed in detail in a previous work [37]; the experimental data investigating the variation of velocity and degree of filling were developed in another study [38].

## 2. Materials and Methods

### 2.1. Material Preparation

The desorbed state of the Li-RHC (represented by the right side of Equation (1),  $2 \text{LiH} + \text{MgB}_2$ ) was selected as starting material adding different amounts of  $\text{TiCl}_3$  (0.005, 0.01, 0.025 and 0.05 mol) as a reaction speed enhancer for the study of the influence of the additive amount. For the experiments about the effect of the different milling parameter, the content of  $\text{TiCl}_3$  under the variation of the BPR was 0.05 mol, while the amount for the tests varying the milling velocity and degree of filling was 0.025 mol. All unprocessed elements were purchased in powder form. The main components, LiH (purity  $\geq 99.4\%$ ) and  $\text{MgB}_2$ , were acquired from Alfa Aesar (Tewksbury, MA, USA). The additive  $\text{TiCl}_3$ , with a level of purity of  $\geq 99.995\%$ , was acquired from Sigma Aldrich (St. Louis, MO, USA). As a reference, three samples were admixed according to Equation (1); one was milled without additive, the others were left unprocessed, but with additive amounts of 0.025 and 0.05 mol of  $\text{TiCl}_3$ .

The powders were treated in a ball mill of the planetary type (Pulverisette 5, Fritsch, Idar-Oberstein, Germany) with different BPR of 40, 20, 10, and 5 to 1. The filling degree of the milling vial varied among 75, 50, 25 and 10%. The maximum time allowed for the milling was 30 h. The tests were executed at several speeds of 330, 230, 130 and 50 rpm. In intervals between 2 and 5 h (according to the other milling parameters) the procedure was paused for 1 h minimum to limit any peak of temperature occurring, while the milling progressed. The milling vials were made with hardened steel and had an internal diameter of 7.6 cm and a depth of about 6.6 cm. Milling spheres were of tempered steel, too, and had a diameter of 1 cm. The material handling and milling processes were completed in a glove box (MBraun, Garching, Germany) under Argon (Ar) atmosphere with  $\text{O}_2$  and  $\text{H}_2\text{O}$  levels under 10 ppm.

### 2.2. Characterizations

#### 2.2.1. Sievert Apparatus

The sorption characteristics of several samples were assessed with a Sievert type apparatus (HERA, Longueuil, QC, Canada) by means of the differential pressure technique. The sample amount for all the experiments was about 200 mg. The purity level of the  $\text{H}_2$  gas used was 99.999%. The samples went through a first total absorption under 50 bar of  $\text{H}_2$  at  $350^\circ\text{C}$  and a desorption under 3 bar of  $\text{H}_2$  at  $400^\circ\text{C}$ . Next, a second similar procedure was executed under the same pressure and temperature settings and used to make an evaluation, as described in the subsequent results section and, with more details, in the supplementary materials. The initial absorption of this RHC has a slow kinetic behavior and so the initial cycle can be considered as “activation”. The cause for this initial slow absorption has not been exactly explained yet, but is also described in the scientific literature (e.g., [39,40]), and is considered in Section 4.2.

#### 2.2.2. X-ray Diffraction

X-ray Diffraction (XRD) method was exploited to recognize the crystalline phases spotted in the sample powders. The experiments were performed using a X-ray diffractometer model D5000

(Siemens, Munich, Germany) using the Cu K $\alpha$  radiation ( $\lambda_{\text{XRD}} = 1.5406 \text{ \AA}$ ). The equipment has a Bragg–Brentano geometry and it is possible to use an airtight plastic sample dome, almost transparent to X-rays, under Ar atmosphere. A low background sample holder was used, with a monocrystalline Si surface with high-index orientation.

The XRD method was useful to calculate the size of the crystallites, as well. These experiments were carried out at the MAX-lab synchrotron situated in Lund (Sweden). All the powders were prepared inside thin-walled quartz glass capillaries, under Ar atmosphere. The measurements were performed in transmission mode with a  $\lambda_{\text{XRD}}$  wavelength of  $0.992 \text{ \AA}$ . These experiments were completed only for the sets of samples considering the milling velocity variation and the degree of filling variation. Uniquely the diffraction pattern of the MgB $_2$  phase was used for the evaluation of the crystallite size, because of the overlapping of the peaks and/or the low intensity coming from the other elements. To calculate the crystallite size  $d$ , the Scherrer Equation [41] was used:

$$d = \frac{K \lambda_{\text{XRD}}}{B \cos \theta} \cdot \frac{180^\circ}{\pi} \quad (2)$$

where  $K = 1$  is a dimensionless shape factor,  $B$  is the full width at half maximum and  $\theta$  represents the Bragg angle. Lattice defects and tensions were neglected, and the instrumental broadening was not considered applying this equation. Therefore, the value for  $d$  is designated only as an approximation and the emphasis is shifted more on the tendency of the values. For this estimation, the most important reflection of MgB $_2$ , at about  $27^\circ$  of  $2\theta$ , was selected.

### 2.2.3. Physisorption Analyzer

The specific surface area (SSA) was calculated applying the Brunauer–Emmett–Teller (BET) method to data retrieved by a Physisorption Analyzer (ASAP 2020, Micromeritics, Norcross, GA, USA). During the degassing, the samples were brought to  $100 \text{ }^\circ\text{C}$  under high vacuum for a period of 20 h. The experiments were carried out at  $77.3 \text{ K}$  with a liquid nitrogen (N $_2$ ) bath. The calculations were applied to relative pressures ranging from 0.3 to  $0.5 p/p_0$ . About 3.5 g of sample were required for each experiment. Therefore, these measurements were performed exclusively for the samples obtained after a total of 30 h of milling time, because the extraction of this amount of powder through the procedure would have influenced the parameters of the milling process significantly (e.g., the BPR and degree of filling).

### 2.2.4. Scanning Electron Microscopy

The material distribution and the surface morphology in the micron range was investigated with an EvoMA10 (Zeiss, Oberkochen, Germany) Scanning Electron Microscope (SEM) with a LaB $_6$  filament. The elemental analysis of the powders was performed by Energy Dispersive X-ray Spectroscopy microanalysis (EDX), by means of a detector INCA Energy 350 X-Max (Oxford Instruments, Abingdon, UK) with a Be window installed. The quantitative elemental analysis is normally calibrated by means of a Cobalt standard. The distribution of the several elements in the areas of the samples was investigated by means of backscattered electrons. To prevent from oxidation, the samples were placed in a special sample holder during the preliminary operations. Therefore, the samples were inserted inside a glove box in this tool and then vacuum was made to transfer the holder to the SEM apparatus. All the SEM experiments were carried out at the Pavia H $_2$  Lab.

## 2.3. Modeling for Energy Transfer Quantification

In a ball mill, including a planetary one, the milling vials are prepared with grinding medium (balls) and then the material to be processed is added. In the course of the process, the vials and the supporting plate are revolving inversely like planets in a solar system (Figure 1).

This rotation causes the milling balls to collide with the milling vial wall and with each other. The powder found in between the grinding medium and between the wall and the balls is crushed this

way and the balls kinetic energy gets transferred to the sample. The energy involved in the process can be tailored changing the milling parameters listed in Table 1.

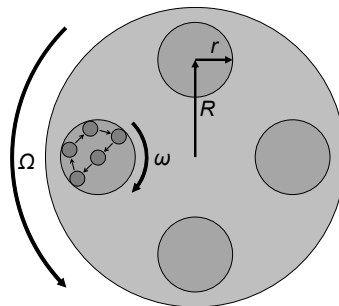


**Figure 1.** Representation of a planetary ball mill, equipped with four milling vials.

**Table 1.** General summary of the milling parameters. *Italic font indicates the variations examined here.*

Label	Milling Parameter	Variation
(a)	Milling time	2 h, 10 h, 30 h
(b)	BPR–Ball-to-powder ratio	5:1, 10:1, 20:1, 40:1
(c)	Velocity	50 rpm, 130 rpm, 230 rpm, 330 rpm
(d)	Degree of filling	10%, 25%, 50%, 75%
(e)	Milling vials/balls material	Tempered steel
(f)	Milling balls diameter	1.0 cm
(g)	Milling vials diameter	7.6 cm
(h)	Milling vials height	6.6 cm
(i)	Type/model of mill	Planetary ball mill (Pulverisette 5, Fritsch)

Supplementary parameters, not further considered in this work, are the atmosphere in the milling vial, the temperature and the addition of milling agents [18]. These additional parameters cause auxiliary effects for the duration of the process (e.g., a gaseous phase inducing reactive milling), but do not affect excessively the transfer of energy to the powders. Here, additional milling agents were not used and the volumes during milling were always filled with Ar gas. Any significant variation in temperature was prevented.

To compute the milling energy, the paths of the grinding spheres have to be estimated and exemplified. Owing to the inverse revolution of the supporting plate and the milling vials, the spheres are presumed to be touching the walls along the half circumference of the internal vial wall and then escape centrifugally to the opposite side of the circle (Figure 1). Agreeing to this hypothetical path, the energy transfer to the powder in the course of the grinding process is calculated using an adapted model, from the original of Burgio et al. [36]. This model accepts that the spheres inside the milling vial neither slide nor roll along the half circumference of the internal wall. The mathematic model is established on the kinetic energy  $\Delta E$  of one ball in the moment of the collision on the wall on the other side of the milling vial:

$$\Delta E = \frac{1}{2} m_b (v_b^2 - v_s^2) \quad (3)$$

The kinetic energy is calculated in this way taking into account the mass of a single ball  $m_b$ , the absolute velocity  $v_b$  of a ball separating from the vial wall and the velocity  $v_s$  after the collision with the opposite side of the vial wall that is equivalent to the velocity of the internal vial wall. The energy transferred during the milling to the powder per unit mass  $P^*$  is provided by the number of spheres and their mutual interactions, by the geometry of the mill device and by the frequency of impacts:

$$P^* = -\varphi_b N_b m_b t (\Omega_p - \omega_v) \left[ \frac{\omega_v^3 \left( r_v - \frac{d_b}{2} \right)}{\Omega_p} + \Omega_p \omega_v R_p \right] \frac{\left( r_v - \frac{d_b}{2} \right)}{2\pi PW} \quad (4)$$

with:

$\varphi_b$  Milling balls interaction (yield coefficient);

$\Omega_p$  Plate absolute angular velocity;

$\omega_v$  Vial absolute angular velocity;

$d_b$  Ball diameter;

$m_b$  Ball mass;

$N_b$  Ball number;

$P^*$  Total transferred power per unit mass (from the milling process to the material);

$PW$  Total weight of the powder;

$R_p$  Vector distance from the mill center to the vial center;

$r_v$  Vector distance from the vial center to the vial wall;

$t$  Total time of milling.

The total milling time  $t$  corresponds to the milling parameter (a) in Table 1. The total weight of the powder  $PW$  is defined by parameter (b); the absolute angular velocity of the ground plate  $\Omega_p$  is expressed by the milling parameter (c), whereas the total number of milling balls  $N_b$  depends on parameters (d), (e), (f) and (g). The mass  $m_b$  and diameter  $d_b$  of one ball are specified by parameters (g) and (h), respectively. The absolute angular velocity of a vial  $\omega_v$  and the vector distances  $R_p$  and  $r_v$  are determined by the type of mill and therefore represent parameter (i). All parameters are shown in Table 1.

An essential parameter is represented by the yield coefficient  $\varphi_b$ , which reflects mainly the percentage of filling. In their work, Burgio et al. [34] assumed a primitive cubic packing of the spheres inside of the milling vial. Even avoiding a formal evaluation of the reliability of this consideration, it is possible to observe through practical trials that the obtained number differs significantly from the actual number of spheres that can be fitted in a vial. In this instance, the model was adapted and a packing arrangement of balls in a hexagonal geometry was proposed. To estimate the maximum number of spheres in a vial ( $N_{b,v}$ ) and number of spheres needed to cover one about 30% of the surface of the inner wall ( $N_{b,s}$ ), Equations (5) and (6), respectively, were modified taking into account the proposed model:

$$N_{b,v} = \frac{\pi r_v^2 h_v}{\left(\frac{d_b}{2}\right)^2 \sqrt{3} \cdot 1,633 \cdot 2 \left(\frac{d_b}{2}\right)} \quad (5)$$

$$N_{b,s} = \frac{2\pi r_v h_v}{6 \left(\frac{d_b}{2}\right)^2 \sqrt{3}} \quad (6)$$

with the height of the milling vial given by  $h_v$ .

### 3. Results

For a better assessment in this work, the time needed to reach 80% of the total transformed fraction of the second hydrogenation and second dehydrogenation is plotted against different milling parameters. This time (in hours) is labelled “ $t_{80}$ ” and is an indication of the kinetic behavior of the reaction. Furthermore, the maximum gravimetric hydrogen capacity after dehydrogenation (here mentioned as “reversible hydrogen capacity”) is plotted and related to the influence of several milling parameters. The motivation for displaying only the  $H_2$  capacity resulting from the desorption reaction is that this value denotes the reversible hydrogen capacity of the RHC after the previous step of absorption. It is important to point out that there was a difference between the two considered values (capacity for absorption and desorption), though it was quite small in all tests. This difference was due to a systematic experimental error.

In Appendix A, additional data of the calculated crystallites size of  $\text{MgB}_2$  and SSA are provided in correlation with the degree of filling and the milling velocity. The results of every single test are displayed with details in the supplementary materials.

In Figure 2a, the data relative to kinetic behavior of the sorption curves shown in Figure S1 are summarized and plotted in correlation to the additive content. The reversible hydrogen capacity from the same set of experiments is shown in Figure 3a, in relation to the amount of additive.

The outcome of the quantity of additive can be noticed by matching the data obtained for different amounts with those for the additive-free sample: the  $t_{80}$  is lowered, and the hydrogen capacity finally reached is improved. Still, by additionally increasing the amount of additive, neither the kinetic behavior nor the  $\text{H}_2$  capacity can be enhanced. The reversible capacity drops and the  $t_{80}$  remains stationary for  $\text{TiCl}_3$  amounts equal to 0.025 mol or higher.

In the other experiments, the additive content is fixed to 0.05 mol when varying the BPR (Figure 2b) and to 0.025 mol when varying the milling velocity and filling degree (Figure 2c,d). In agreement with the results above, the kinetic behavior should not be considerably influenced by the difference of these amounts.

The effect of the ball-to-powder ratio on the kinetic behavior is represented in Figure 2b, where the  $t_{80}$  for both absorption and desorption are shown, against the BPR, for different milling times summarizing the data retrieved from the several graphs of Figure S2, where the other detailed parameter can be found.

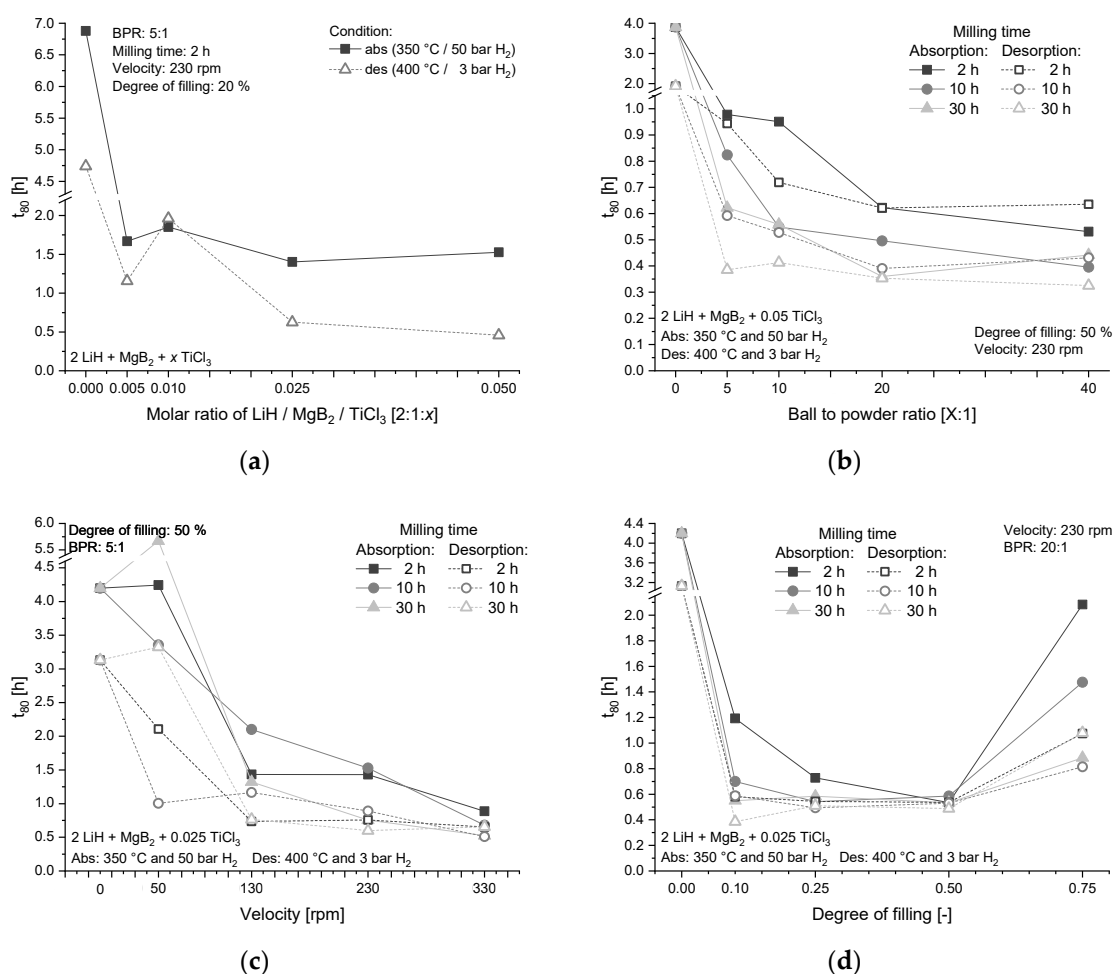


**Figure 2.** Kinetic behavior, expressed by means of  $t_{80}$ , as function of (a) additive content, (b) BPR, (c) milling velocity, and (d) degree of filling. All sets are for absorption and desorption, and display different milling times.

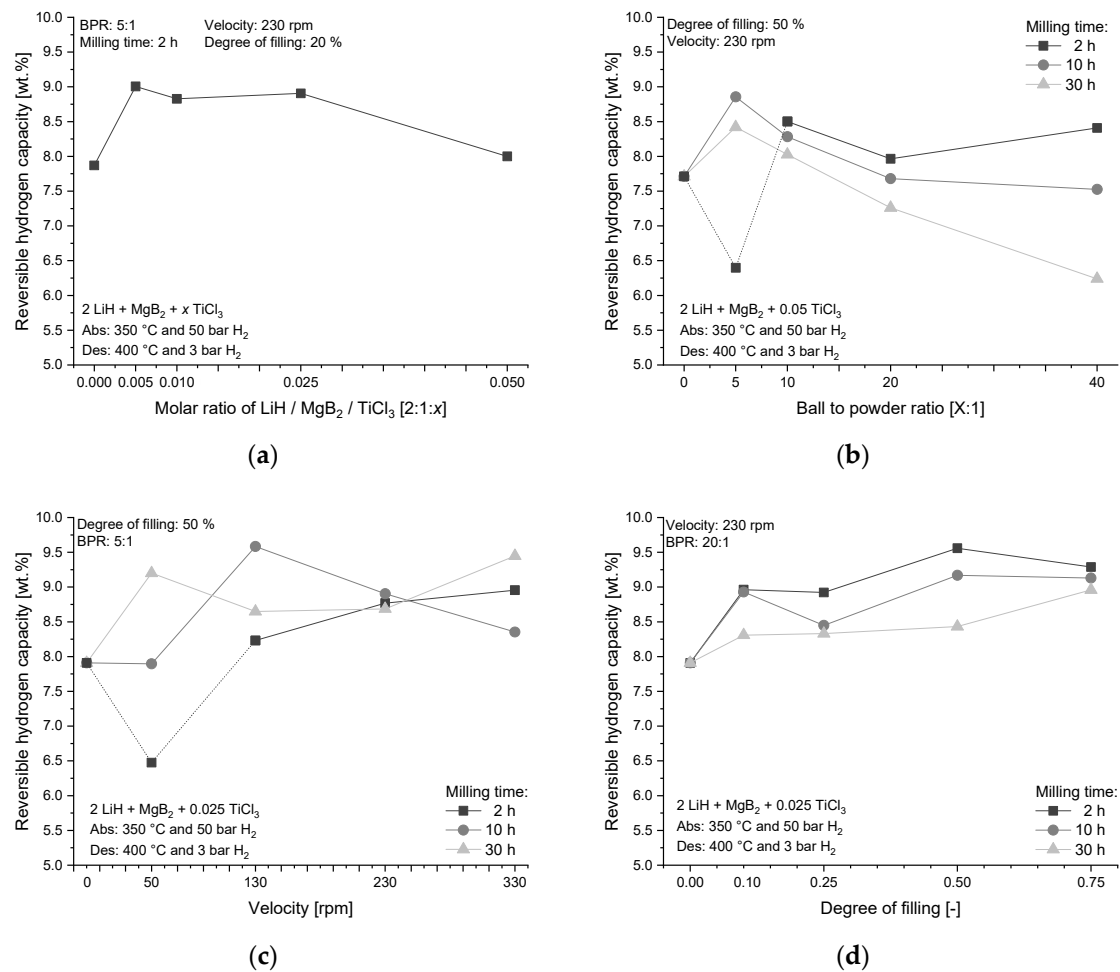


**Figure 3.** Reversible capacity of hydrogen after desorption as function of (a) amount of additive, (b) BPR, (c) milling velocity, and (d) degree of filling. Some sets display different milling times, too.

A BPR of 5:1 already displays a significant improvement in the kinetic behavior for the hydrogenation and dehydrogenation in comparison to the not milled sample (designated in the graphs by the symbol relative to a BPR of 0:1). The milling time influence on  $t_{80}$  is comparable for all the considered BPR. Increasing this time, the kinetic rate is faster or nearly at the same rate as the previous case. The kinetic behavior also improves increasing the BPR, though this effect is highly noticeable for shorter grinding times. With a processing time longer than 30 h, the effect of the BPR becomes almost insignificant, in particular for the dehydrogenation reaction. In Figure 3c, the effects of the milling time and the BPR are shown for the reversible hydrogen capacity. A clear tendency is also evident for the influence of these two parameters on the H<sub>2</sub> capacity. This is true with the exception of a 5:1 BPR after 2 h of process, which is presumably partly oxidized because of the lower displayed capacity, when compared to the other data. As an initial consequence of the milling process, an increased capacity was expected, but with a longer milling time and also a higher BPR, the capacity gets lowered again. It is possible to notice this trend for milling times longer than 2 h.

To understand how the milling velocity influences the kinetic behavior of the processed powders, this resulting parameter is shown in correlation with different milling times and velocities in Figure 2c for the absorption and desorption. The original experimental curves and the complete parameters are displayed in Figure S3. For the process at 50 rpm, at different milling times the  $t_{80}$  values change significantly. A distinct effect of the milling process on the kinetic behavior cannot be perceived at this velocity, compared to the not milled sample, for both absorption and desorption. A trend of the influence of milling time on the kinetic behavior is also not clearly noticeable for the entire set of

velocities. With the exception of the experiment at 50 rpm, the graphs for  $t_{80}$  with different processing times are similar to one another.

The influence of the milling velocity on the hydrogen storage capacity is reported in Figure 3c. Regarding the influences of the milling time and of the velocity on the reversible H<sub>2</sub> capacity for process durations of 10 and 30 h, it is not possible to notice a clear trend. However, the hydrogen capacities result on average slightly higher than that of the unmilled sample. The reversible capacity increases with a higher milling velocity after 2 h of milling, with the exception of the powder milled at 50 rpm, due to the alleged limited oxidization discussed before. The final absolute values are all approximately 9 wt.%, with an unclear trend along the x-axis as opposed to the results acquired with the BPR variation (Figure 3b).

Figure 2d shows the effect of the degree of filling on the hydrogenation and dehydrogenation kinetic behavior, condensing the results from the tests described in the graphs of Figure S4.

Obviously, the processes with 0% of milling media exhibit the worse  $t_{80}$  values; an increase of degree of filling displays an optimal trend for the kinetic behavior of the absorption, similar for all processing times, at a filling degree of 50% of. For process durations of 10 h and 30 h, the same kinetic value can be obtained already at 25% and 10% of filling, respectively. For the dehydrogenation reaction, the total processing time seems to have a smaller influence and, thus, the optimal interval goes from 10% to 50% of vial filling.

The effect on the hydrogen capacity of the degree of filling is displayed in Figure 3d. Again, the final capacity was slightly enhanced due to the grinding process in comparison to the not milled reference and a negative inclination is not noticeable increasing the degree of filling, though increasing the process time, this enhancement is less prominent and the reversible capacity is lower. An optimal result can be seen also at 50% of filling for 2 h and 10 h of milling time. Once more, the variations of the absolute values are on a higher range if compared with the previous results (Figure 3b,c) with a mean value of 9 wt.%.

#### 4. Discussion

In the following section, the discussion is focused on the influence of several parameters on the total amount of energy transferred to the powder during milling (Section 4.1). The application of the modified model allowed calculating the total transferred energy and easily comparing the results with other milling techniques, even at different batch sizes. Additionally, it is possible to assess the different milling parameters according to their separate effect on the transferred energy. The influences on the kinetic behavior and hydrogen capacity are discussed and the obtained results are shown in Sections 4.1.1 and 4.1.2. Further elements for the discussion are provided by the SSA of the milled powder composite and by the calculated crystallite sizes of MgB<sub>2</sub>, in Appendix A. Finally, along with the outcomes acquired for different amounts of additive and the SEM micrographs, just the impact of the additive, combined with the ball grinding process, is analyzed in Section 4.2.

##### 4.1. Transferred Energy During Milling

In agreement with Equation (4), any increase in the milling time, velocity, BPR or degree of filling, means an increase of the total transferred energy. Thanks to the amendments in Equations (5) and (6), the agreement between empirical measurements and calculated number of balls in one vial was noticeably improved: the standard deviation was reduced from 24% to 7% by presuming a hexagonal arrangement as a replacement for a primitive cubic one.

The resulting theoretical relationship is analyzed and validated with the experimental data from Section 3, both for the kinetic behavior and for the hydrogen capacity in Sections 4.1.1 and 4.1.2, respectively.

#### 4.1.1. Influence on Kinetic Behavior

Different milling parameters can change the energy transferred to the material upon milling. Thus, the changes of the theoretical transferred energy for each experiment was determined with Equation (4). Results of the absorption kinetic behavior ( $t_{80}$ ) are compared for the different BPRs in Figure 4a, the different velocities in Figure 4b and the different degrees of filling in Figure 4c.

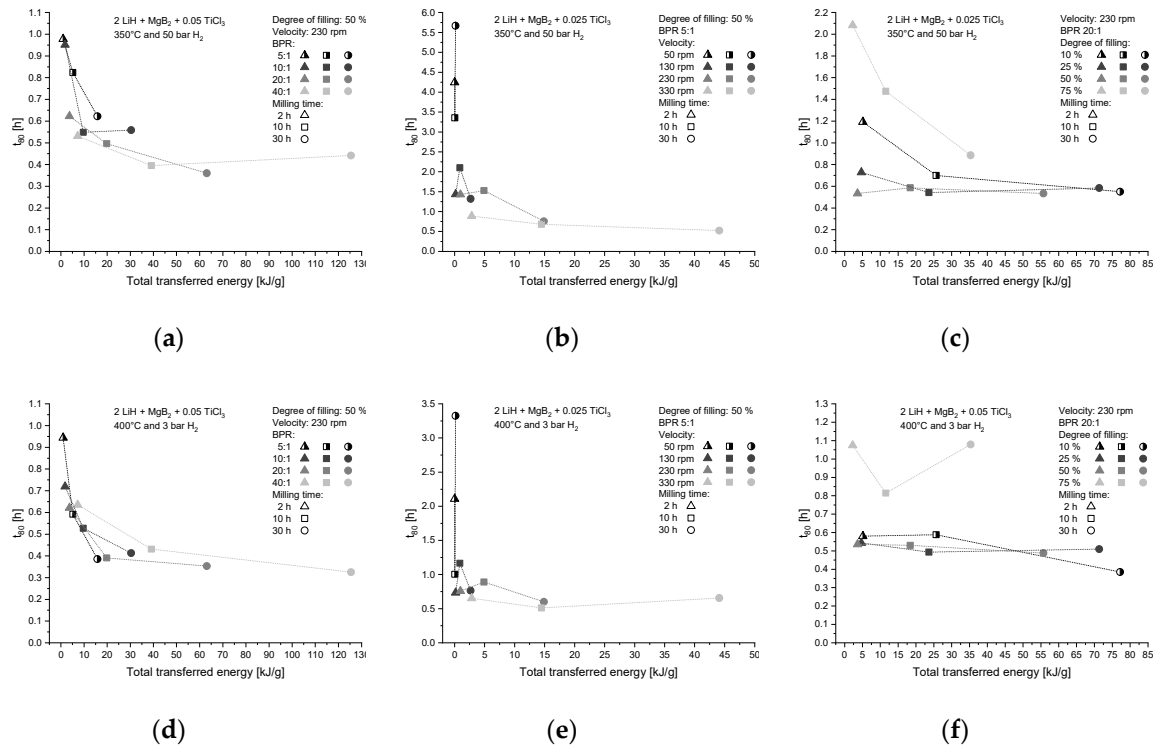


**Figure 4.** First row: absorption kinetic behavior as a function of the energy transfer for different (a) BPRs, (b) milling velocities and (c) degree of filling, as well as for different milling times. Second row: graphs related to desorption  $t_{80}$  varying (d) BPRs, (e) milling velocities and (f) degree of filling.

The parameter  $t_{80}$ , displayed as a function of the energy transfer, drops exponentially for the different velocities and BPRs, and then reaches stable values between 0.45 and 0.65 h. The enhancement of reaction kinetics can be ascribed, as mentioned above, to the greater energy transfer to the material resulting from the higher BPRs, higher milling velocities and times chosen. Though, the different degrees of filling (Figure 4c) do not behave following this connection entirely; the causes are discussed further on. With the variation of the BPR, the transferred energy changed up to 130 kJ g<sup>-1</sup> from few kJ g<sup>-1</sup>. The choice of a higher milling velocity brings the energy values to 45 kJ g<sup>-1</sup> and lastly the degree of filling can increase the energy up to 80 kJ g<sup>-1</sup>. Nevertheless, the lower energies obtained varying of the milling velocity are controlled by the low value for BPR. The important effect of this ratio on the total energy transfer can be noticed in Figure 4a.

To analyze the relation between the transferred energy and the  $t_{80}$  for desorption, the same comparisons as those displayed in the first row of Figure 4 were made. The correlated graphs are plotted in the second row for the different BPRs (Figure 4d), milling velocities (Figure 4e) and degree of filling (Figure 4f).

As with the absorption, the desorption  $t_{80}$  is exponentially lowered with the change of the milling velocity and the BPR, until stable values are reached between 0.4 h and 0.5 h. A clear trend cannot be completely noticed in the case of measurements with different degrees of filling (Figure 4f), so this parameter underwent a correction reported in Appendix B.

As a further amendment, the result at 50 rpm in Figure 4b and e are ignored due to the low transferred energy (0.010 to 0.157 kJ g<sup>-1</sup>) in contrast to the other resulting energies transfer. The difference of the  $t_{80}$  levels at 50 rpm is just considered as a statistical variation. The results for 50 rpm of velocity and 75% of filling are therefore ignored in the next lines. The results for both hydrogenation and dehydrogenation are summarized in Figure 5a,b, respectively.

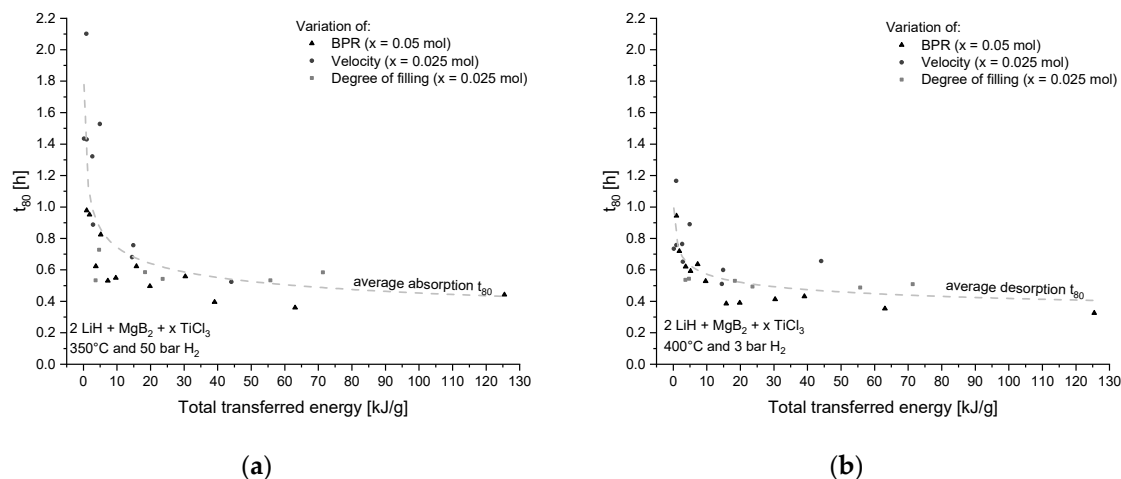


**Figure 5.** Kinetic behavior as a function of total energy transfer considering different milling parameters for (a) absorption and (b) desorption.

Figure 5a,b show that, without regard to the considered milling parameter, the correlation between the average reaction kinetics and the total energy transferred into the powder is represented by a power function, for both the absorption (Figure 5a) and the desorption (Figure 5b) reactions. The improvement of the kinetic behavior, for both reactions, is remarkable up to approximately 20 kJ g<sup>-1</sup>; over this value, the kinetic behavior can only be slightly enhanced with an additional increase of energy. The effect on the hydrogenation reaction is more significant than on the dehydrogenation. This is because for hydrogenation the values present a wider distribution along the  $y$ -axis. The cause for this phenomenon is analyzed in Section 4.2.

Based on the results shown, an optimal set of milling parameters can be chosen to target a desired reaction kinetic.

#### 4.1.2. Influence on Hydrogen Storage Capacity

Figure 6 shows a summary of the effects of different milling parameters on the reversible hydrogen capacity (second cycle). The H<sub>2</sub> capacity is displayed in correlation with the energy transfer, in agreement with the parameters from Equation (4), for several BPR (Figure 6a), velocities (Figure 6b) and degrees of filling (Figure 6c).

The H<sub>2</sub> capacities for 2 h of milling and a BPR of 5:1 (in Figure 6a) and for 2 h of milling and 50 rpm (in Figure 6b) were not considered, because of the partial oxidation mentioned before. The same adjustments considered in the previous section were used for the degree of filling, In particular for the value of 75% in Figure 6c. There is a visible negative trend for tests performed at high transfer of energy (Figure 6a,c). In the case of experiments carried out at lower transfer of energy (Figure 6b), the hydrogen capacity is almost stable. Figure 7 summarizes all measurements.

The influence of the energy transferred by processing on the H<sub>2</sub> capacity of the material is not straightforward. On the one hand, the value presents stable trend for energies up to approximately 30 kJ g<sup>-1</sup>. On the other hand, the capacity is lowered over this value. In Figure 7, the decrease in the capacity is indicated by the dashed line. In the following section the reasons of this negative trend are explained.

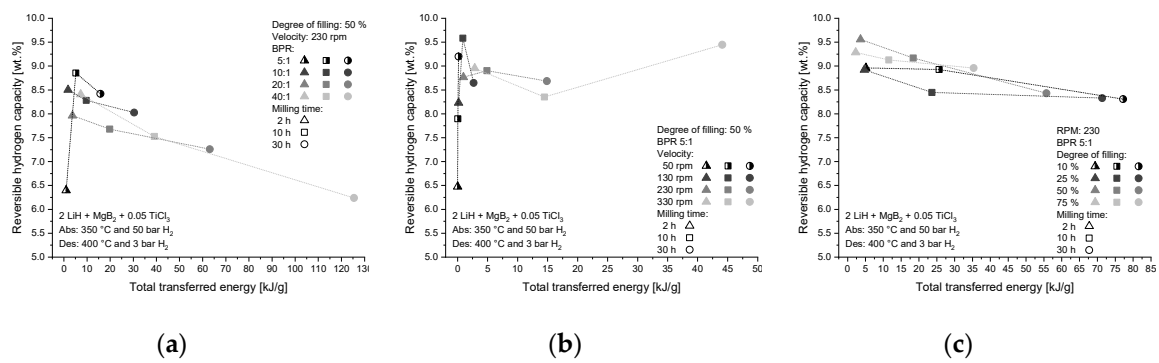


**Figure 6.** Reversible hydrogen capacity as a function of total transferred energy for different milling times as well as (a) BPRs, (b) milling velocities, and (c) degree of filling.

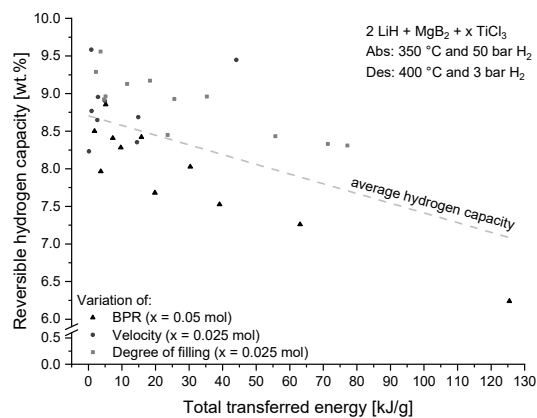


**Figure 7.** Hydrogen capacity (reversible) as a function of energy transfer, considering all the different milling parameters.

#### 4.2. Effect of Additive and Milling

The reaction kinetics (Figure 2a) and the partially reduced hydrogen capacity (Figure 3a) can be enhanced by adding  $\text{TiCl}_3$  to the  $2 \text{LiH} + \text{MgB}_2$  composite, as mentioned in Section 3. Concurrently, the kinetic behavior can be further improved increasing the milling energy, while the  $\text{H}_2$  storage capacity is lowered. In previous sections, the effect of the energy transfer on the reaction kinetics and on the hydrogen density was thoroughly discussed and their connection was defined respectively by a negative exponent power function and a negative slope linear function. The improvement of the kinetic behavior can be explained by two reasons: (i) the reduction of the sizes of particles and crystallites and (ii) the even distribution of nucleation sites. These two aspects are analyzed in detail in the following sections. The reduction of the storage capacity with the increase of milling energy is probably caused by the increase of Fe contaminations. The collisions between the milling balls and the vial wall lead to abrasion of the hardened steel, which can cause an Fe contamination. This can be clarified easily with the lower value of hardness of the steel, in comparison to the ones of  $\text{TiB}_2$  and  $\text{MgB}_2$  (highly available in the vial), as listed in Table 2.

**Table 2.** Knoop hardness (HK) for the different compounds used in the process.

Material	HK	Ref.
Hardened steel 1.3505	776	[4]
LiH	~67	[4,42]
Mg	~40	[43]
$\text{MgB}_2$	1800	[4]
$\text{TiB}_2$	2850	[4]

The presence of  $TiB_2$  in the compound will be discussed in the following section. The iron contaminations reduce the relative hydrogen capacity because the milled mass increases. Puzkiel et al. [44] investigated the effects of Fe on the Li-RHC. Equilibrium thermodynamic calculation and experimental evidence showed that the interaction between Li-RHC and Fe leads to the formation of the FeB phase. This transition metal boride remains upon hydrogen cycling leading to a loss of capacity and a detrimental effect on the kinetic behavior of the material.

#### Nucleation Sites and Iron Contamination

The theory of a better distribution of the additive after milling, discussed above, can be confirmed comparing the SEM micrographs obtained with backscattered electrons for a not milled sample (Figure 8a) with the ones of a milled sample (Figure 8b).

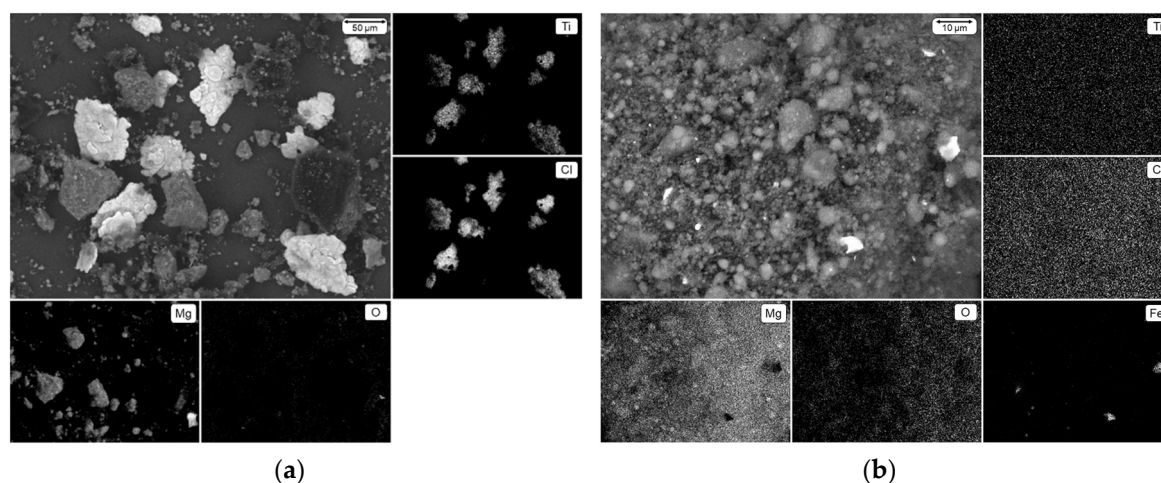
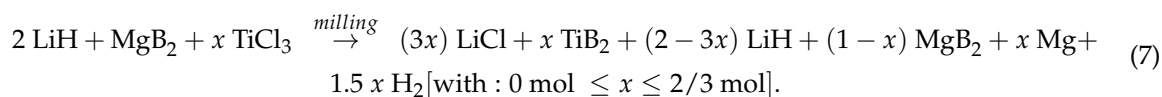


**Figure 8.** SEM backscattered electrons micrographs of the  $2 LiH + MgB_2 + 0.025 TiCl_3$  composite (a) for the unmilled sample, with EDX maps for Mg, O, Cl and Ti, and (b) for a sample milled at 330 rpm for 30 h with 50% of filling and a BPR of 5:1, with EDX analysis for Mg, O, Fe, Cl and Ti. Adapted from Reference [45], with permission of Elsevier, 2015.

Before milling, large particles and agglomerates of the additive  $TiCl_3$  and of  $MgB_2$  can be observed in the SEM images in Figure 8a; there, the existence of unreacted  $TiCl_3$  can be suggested overlapping the Ti and Cl elemental analysis. The presence of  $MgB_2$  can be assumed in Figure 8a just by the elemental analysis of Mg, since B (together with H and Li) is a too light element to be detected with this method. For this reason, also LiH cannot be identified. The oxidation of the components is moderately low, agreeing to the analysis for O, and it takes place presumably on the particles surface only. The low oxidation extent both before and after the process (Figure 8a,b) may occur during the transport of the sample from the glove box respectively after the mixing or grinding and is not expected to happen during the process itself.

After the milling process, the components are effectively distributed, as it can be noticed from the elemental analysis for Mg, Cl and Ti. By XRD analyses in Figure 9, it is possible to observe that LiCl is present after milling and remains after cycling. Moreover, the presence of Ti or Ti bases compound is not detected (Figure 9).

In a previous work [30], the formation of stable  $TiB_2$  upon milling following the following reaction mechanism (7) has been already proposed:



The formation of  $1.5 x$  mol of gaseous  $H_2$  is predictable, by solving the stoichiometric equation. This quantity of hydrogen is released as gas during milling and therefore not shown as a product in the above equation. Hence, the additive reacts to form titanium boride ( $TiB_2$ ) and lithium chloride ( $LiCl$ ) during milling, which are anticipated to be highly and homogeneously distributed [16,32,33,46]. The formation of  $TiB_2$  was verified via the combination of advanced techniques such as high resolution-transmission electron microscopy (HR-TEM), extended X-ray absorption fine structure (EXAFS) and X-ray absorption near-edge structure (XANES), due to its nanocrystalline nature [32,33,40,46].

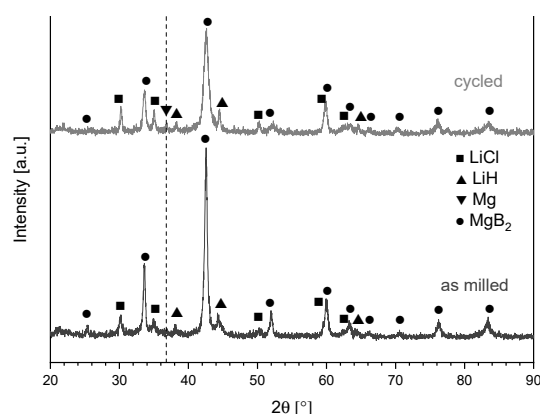


**Figure 9.** XRD patterns for the  $2 LiH + MgB_2 + 0.025 TiCl_3$  composite milled for 30 h at 330 rpm with 50% of filling and a BPR of 5:1 before (as milled) and after 2 cycles (cycled). Adapted from Reference [30], with author's permission.

This can be observed also by the additional presence of Mg after cycling (see Figure 9). It could also explain the difference in the kinetic behavior between the initial and the following absorption. Up to now, only the second hydrogenation and dehydrogenation reactions have been evaluated for comparison in this work, as a strong improvement was observed with respect to the first cycle, thus considered as an activation step. This improvement is clearly displayed in Figure 10a. For the desorption process, displayed in Figure 10b, the reaction rate is similar for both cycles.

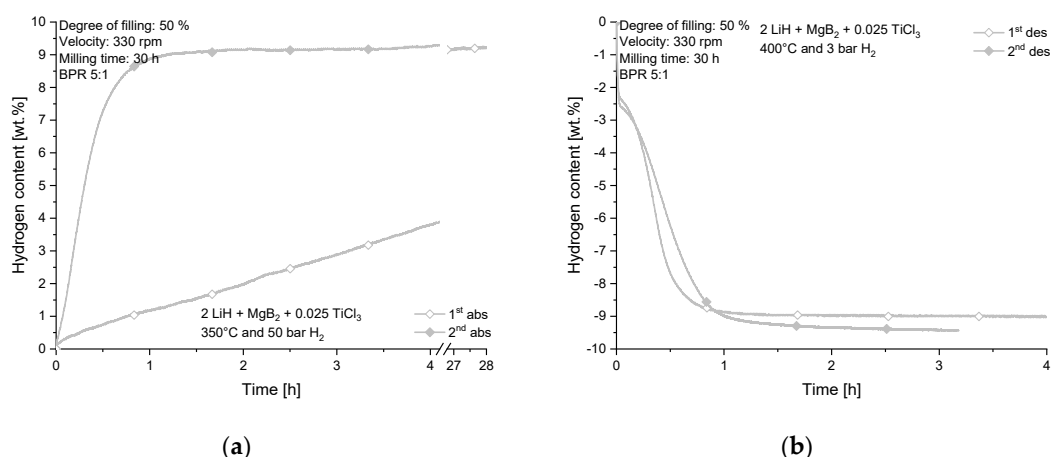


**Figure 10.** Hydrogen quantity against time for a powder sample milled for 30 h under 330 rpm with a 50% of filling and a BPR of 5:1 for (a) absorption and (b) desorption.

The first hydrogenation reaction takes approximately 28 h to reach the maximum hydrogen quantity. In the second hydrogenation, the kinetic behavior enhances and it takes just 1 h to reach the full capacity. This evidence suggests that decreasing particle and crystallite sizes, and thus shortening the diffusion pathways, is not enough to clarify the influence of the milling process

and of the additive, as it would be noticeable already for the initial absorption. Besides this effect, the presence of homogeneously dispersed  $\text{TiB}_2$  as heterogeneous nucleation sites (due to the low interplanar and directional misfit with the hexagonal crystal lattice of  $\text{MgB}_2$ ) after the initial absorption enhances the reaction kinetic. The effective distribution means an additional crystallite refinement; this phenomenon, owed to boron compounds (particularly  $\text{TiB}_2$ ), has been already described in literature [47–49]. According to Figure 2a the number of nucleation sites appears to display a maximum already for a content of  $\text{TiCl}_3$  equivalent to 0.025 mol per mole of  $\text{MgB}_2$ .

The drawback for an improved dispersion of the additive (Figure 8b) during the process and the reduction of the particle and crystallite sizes (according to Appendix A), is the increase in Fe-contamination, as already mentioned before. This iron contamination is noticeable in the SEM micrograph after milling (Figure 8b), but did not exist before (Figure 8a). However, it was not observed in the XRD (Figure 9) after milling or after cycling. The cause for this absence could be the theory of the formation of broader iron particles mentioned above, providing a rarer occurrence in XRD analysis.

## 5. Conclusions

The increase of the milling time, BPR and velocity for 2 LiH +  $\text{MgB}_2$  (plus additive) leads to a higher energy amount transferred to the powder material. In addition, a change in the degree of filling of the vials with material and balls leads to an improvement in the hydrogen absorption and desorption properties, but only when the parameter falls in the range from 10% to 50%. Therefore, the energy model needs to be adapted for this parameter. In addition, the diameter of the milling spheres should be investigated, as one of the last milling parameters not studied in this work.

The transferred energy could be calculated between few  $\text{kJ g}^{-1}$  to  $130 \text{ kJ g}^{-1}$ , and an amount of  $20 \text{ kJ g}^{-1}$  might be already considered enough for a marked enhancement of the reaction kinetics. A higher amount of transferred energy results in improved reaction kinetics, but simultaneously causes a degradation of the  $\text{H}_2$  capacity.  $\text{TiCl}_3$  was investigated as additive component. The enhancement in reaction kinetics thanks to the additive and the milling process itself could be explained by: (i) the homogeneous distribution of nucleation sites and (ii) the reduction of particle and crystallite size. After the milling process, the size of the particles can be decreased to a few micrometers and the crystallite one to some nanometers. This promotes the reaction due to lower diffusion barriers. Highly distributed  $\text{TiB}_2$  particles, which form after the first absorption, could be observed and considered as nucleation sites for  $\text{MgB}_2$ . The decrease in the hydrogen capacity is predicted to be due to the increasing friction and wear of the milling tools (steel spheres and vial) with processing. This phenomenon might be improved using harder milling tools (e.g., made of tungsten carbide).

The kinetic behavior enhancement achieved including the additive reaches the maximum for a molar ratio for LiH,  $\text{MgB}_2$  and  $\text{TiCl}_3$  of 2:1:0.025. In conclusion, an optimal set of additive content and milling parameters, consisting of time, milling velocity, BRP and degree of filling, were determined and could be employed, thanks to the broad validity of the energy model, for different milling processes and scaled up production.

**Supplementary Materials:** The following are available online at <http://www.mdpi.com/2075-4701/9/3/349/s1>, Figure S1: Transformed sorption fraction for different additive contents, Figure S2: Transformed sorption fraction for different BPR, Figure S3: Transformed sorption fraction for different milling velocities, Figure S4: Transformed sorption fraction for different degrees of filling.

**Author Contributions:** The authors contributed as follows: conceptualization, J.J. and G.C.; methodology, J.J.; investigation, N.B., T.W. and A.G.; data curation, J.J., N.B., T.W., C.M. and A.G.; formal analysis, J.J. and J.P.; validation, J.J., G.C., J.P. and C.M.; visualization, J.J. and G.C.; writing—original draft, J.J., G.C. and J.P.; writing—review & editing, G.C., J.P. and C.M.; supervision, J.J. and J.B.v.C.; resources, C.M., M.D. and T.K.; project administration and funding acquisition, M.D. and T.K.

**Funding:** This research received no external funding.

**Acknowledgments:** The authors are grateful to the Alexander von Humboldt Foundation in the frame of the post-doctoral fellowship of J.P. (No: ARG-1187279-GF-P); J.P. thanks CONICET (Consejo Nacional de Investigaciones Científicas y Técnicas).

**Conflicts of Interest:** The authors declare no conflicts of interest.

## Appendix A

In this appendix, additional data and discussion about the specific surface area and the calculated crystallite size of  $\text{MgB}_2$  are provided. Respectively in Figure A1a,b, there are the representations of these properties in correlation to the milling velocity and to the degree of filling.

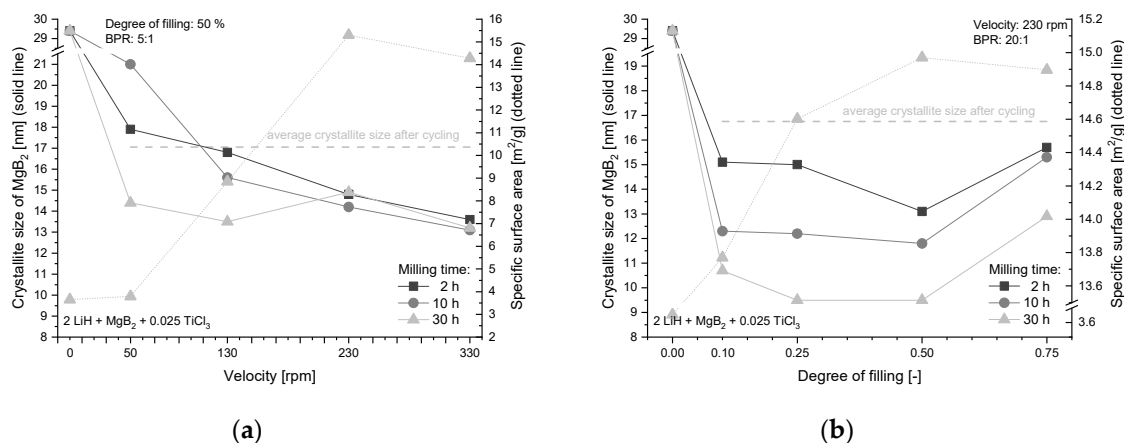


**Figure A1.** Crystallite size of  $\text{MgB}_2$  (calculated) and specific surface area of powders, as a function of (a) the milling velocity and of (b) the degree of filling, for different milling times.

In the same way for the kinetic behavior and the capacity, and also for the milling time, no marked tendency of the influence on the calculated  $\text{MgB}_2$  crystallite size can be detected. For the top milling velocities considered (230 and 330 rpm), the effect of the processing time appears to be almost negligible. In the beginning, the grinding process leads to a strong decrease of the crystallite size, even just at 50 rpm for all processing times. This size is additionally decreased with the velocity for process times equal to 2 h and 10 h, whereas this change is practically absent for 30 h of process. At this same value of milling time, the SSA increases, with velocities higher than 50 rpm, and reaches a local plateau of about  $15.5 \text{ m}^2 \text{ g}^{-1}$  around 230 rpm. Between the value for the unmilled reference powder and the one processed at 50 rpm, the SSA appears to be similar. The crystallite size after  $\text{H}_2$  cycling is nearly unvaried, independently from the value obtained after milling, with an average size of 17 nm, as calculated by measuring this parameter for all the samples shown in Figure A1b, after two cycles of hydrogenation and dehydrogenation.

The impact of the filling degree on the calculated  $\text{MgB}_2$  crystallite size and on the SSA is displayed in Figure A1b. Analogous to the kinetic behavior and the reversible  $\text{H}_2$  capacity, the variations in the calculated crystallite size are noteworthy, for a filling of 10% already. With a higher content of milling material, the  $\text{MgB}_2$  crystallite size does not vary up to a filling of 50% and increases afterwards, for 10 h and 30 h of processing. For 2 h of milling process, a local minimum is present at a filling level of 50%. Generally, the crystallite size decreases with an increase of the milling time, not depending on the level of filling. After sorption cycling, the mean crystallite size of the samples processed for 2 h at filling degrees of 10% and 50% was determined to be 17 nm. In agreement with the results acquired for the deviation of the milling velocities, this value is once more comparable, after cycling, for all the levels of filling.

The predictable impact of higher milling energy is the shrinkage of diffusive paths, owing to reduced crystallite and particle sizes, as stated above. The determination of the SSA in the previous paragraphs was used to approximate the particle size. In this manner, it is expected that with an increase of surface area, as the resulting particles are expected to be not largely porous, the particle size would decrease. Agglomeration during the process leads to a decrease in surface area that was not verified in case of the studied samples (Figure A1a,b). Under the assumption of a homogenous

particle size distribution, no sintering or agglomeration, and a spherical shape with smooth surfaces, the particle size  $d_{\text{particle}}$  can be estimated from the SSA value applying Equation (A1):

$$d_{\text{particle}} = \frac{6}{\rho_{\text{solid}} \cdot \text{SSA}} \quad (\text{A1})$$

The determination of the theoretical density for the solid composite  $\rho_{\text{solid}}$ , was displayed in a previous work [50] without the addition of  $\text{TiCl}_3$ . The calculated particle size is displayed in Figure A2 versus the absorption (Figure A2a) and desorption kinetic (Figure A2b).

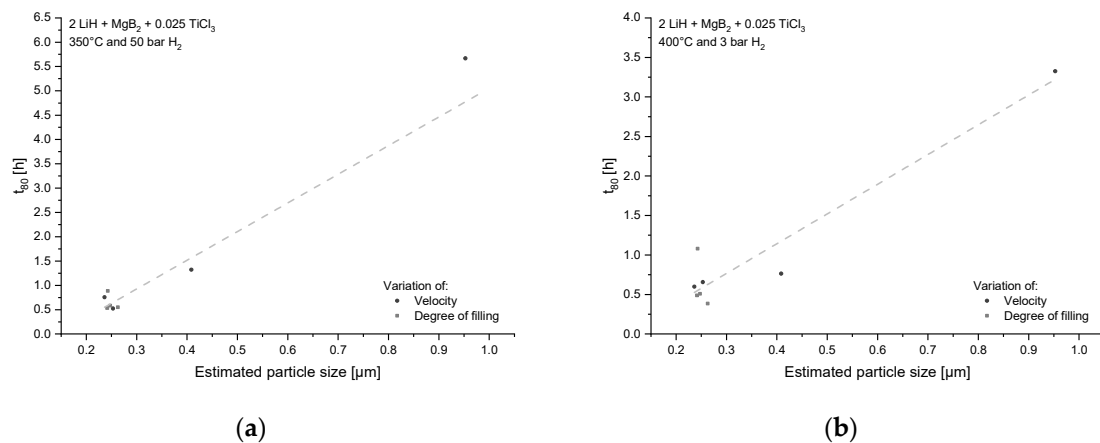


**Figure A2.** Kinetic behavior as a function of calculated particle size after grinding for (a) absorption and (b) desorption.

Agreeing to the hypothesis made in Equation (A1) and the reported values for the SSA in the beginning of the appendix, the calculated mean particle size of the material after processing ranges from 0.25 to 1  $\mu\text{m}$ . The hydrogenation and dehydrogenation kinetic represented in correlation with the particle size displays a hint of a linear behavior. The reaction kinetic of both hydrogenation and dehydrogenation is improved with reduced particle size.

By examining several powder samples with the help of SEM (for example, an unmilled and then a milled powder in Figure A3a,b) the assumptions used for the calculation of the particle size can be deemed as not valid and there is the need to adjust (or rather consider as average ones) the absolute values. Nevertheless, the simple correspondence between kinetic behavior and particle size should not be altered.

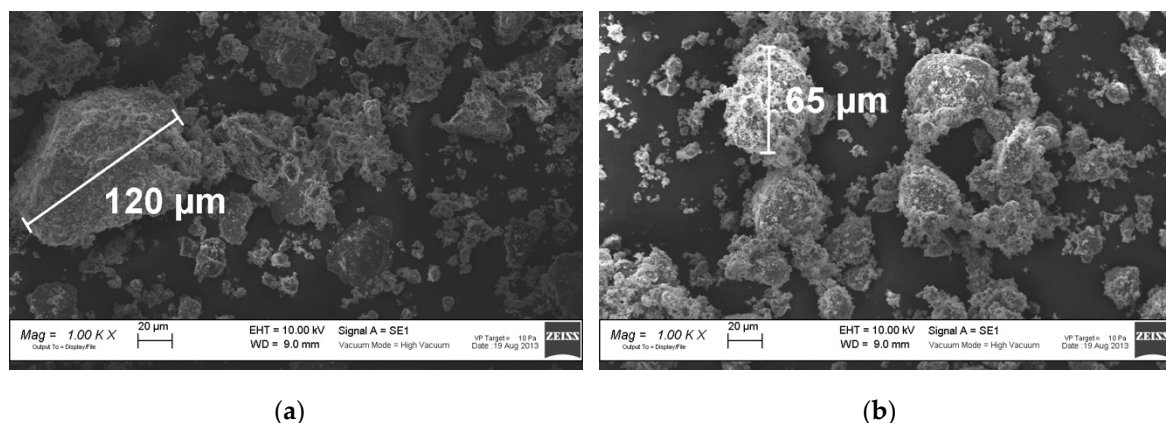


**Figure A3.** SEM image of  $2 \text{ LiH} + \text{MgB}_2 + 0.025 \text{ TiCl}_3$ : (a) an unmilled sample and (b) a sample milled at 330 rpm for 30 h with 50% of filling and a BPR of 5:1.

The shape and the size distribution of the particles are highly inhomogeneous and their surfaces are irregular. Moreover, possible agglomerates can be observed in the milled powder, even if it is hard to differentiate between agglomerations and oddly shaped particles applying this technique. The maximum dimension of these agglomerates/particles is approximately two orders of magnitude bigger than the  $d_{\text{particle}}$  size estimated starting from the SSA values, even though the influence of processing is also perceptible in the SEM pictures. The largest agglomerates/particles measured before the milling process were almost 120  $\mu\text{m}$  large and they could be grinded to maximum 65  $\mu\text{m}$  upon milling. The hypotheses stated before were made just to obtain an approximation of the  $d_{\text{particle}}$  size and analyze the trend more than the values themselves. Alternative methods to measure more precisely the particle size, e.g., laser diffraction, are not applicable, due to the need to disperse the sample inside a fluid carrier, which could react with the powder and change the particle size consequently. In agreement with the results obtained, a link between the reaction kinetics and the after-process particle size, with a Gaussian distribution from several nanometers to tens of micrometers, was presumed. The results match well with the ones obtained for the particle size distribution of milled  $\text{MgH}_2$  [51]. Theoretically, the smallest particle size is specified by the crystallite size. The average value for  $\text{MgB}_2$  after  $\text{H}_2$  cycling results about 17 nm, independently from the starting size. Hence, it can be expected that the kinetic behavior is not influenced by the original crystallite size. Though, a clear association between the original crystallite size and the absorption kinetics can be observed in Figure A4a. A similar correspondence happens also for the dehydrogenation reaction, as displayed in Figure A4b.

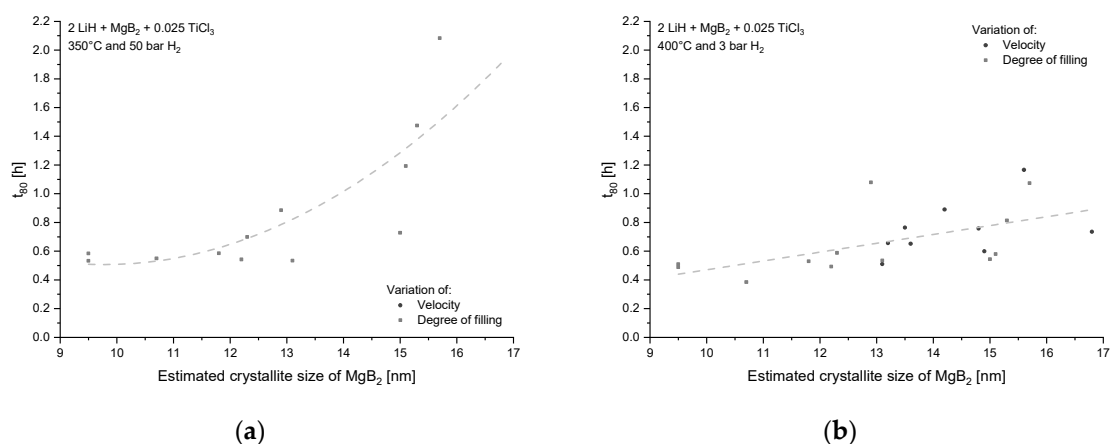


**Figure A4.** Kinetic behavior as a function of the calculated  $\text{MgB}_2$  crystallite size after processing for (a) absorption and (b) desorption.

The absorption kinetic behavior can be enhanced lowering the original crystallite sizes after processing to 12 nm, for  $\text{MgB}_2$ . Below this value, the absorption  $t_{80}$  can hardly be further enhanced. For the dehydrogenation, the relationship between the reaction kinetics and crystallite size displays an approximate linear trend. The values of crystallite size converge to a constant one after  $\text{H}_2$  cycling. This phenomenon could be explained with the phase change occurring to boron, from the solid  $\text{MgB}_2$  to the liquid  $\text{LiBH}_4$  and back. Even though the crystallite size is changing with cycle repetitions, the connection between  $t_{80}$  and initial crystallite size suggests a homogeneous dispersion of the component materials and thus explains the development of the kinetic behavior. A smaller crystallite size suggests an increased plastic deformation and therefore an improved distribution of the additive. This was described in detail in Section 4.2.

The results discussed to this point consider only the impact of milling process on the crystallite size of  $\text{MgB}_2$ . The influence on the size of LiH crystallite is not defined, because the Knoop hardness of LiH is much lower than  $\text{MgB}_2$  (Table 2). This more ductile behavior would be expected, as verified

already for Mg [52], having a similar hardness value. Still, a constant crystallite size after cycling is also an expected effect, owing to the phase change of lithium from solid LiH to liquid LiBH<sub>4</sub> and back.

Developing this argumentation, it is strongly probable that the kinetic behavior of the Li-RHC can be enhanced by reducing both crystallite and particle size, as a result of increasing the milling process energy and minimizing the barriers for diffusion.

## Appendix B

This appendix deals with a correction necessary for the degree of filling. In agreement with Equation (4), a higher degree of filling leads to a lower amount of transferred energy and this decrease is continuous with the increase of the filling level. This theoretic association, founded on Equations (5) and (6), results in a nearly linear trend with a slightly curved shape. Still, the proposed hypotheses were inaccurate and the  $t_{80}$  data displayed in Figure 2d show that, in place of a decreasing curve, the relationship between the degree of filling and the process energy is well represented by a distribution function with asymmetrical features and a plateau. This appears after a sudden increase in the lower region below 10%, then the yield coefficient is approximately 1 in a flat maximum and finally it presents a decrease after a filling degree of 50%, as sketched in Figure A5.

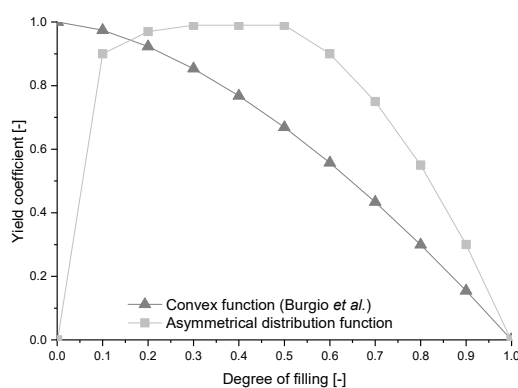


**Figure A5.** Yield coefficient of the process in correlation to the degree of filling.

Therefore, with a translation of the curves in Figure 4c,f for 75% of filling towards lower energy values, the exponential shape matches the abovementioned results for the variation of milling velocity and of BPR. On the one hand, the reason for an asymmetrically shaped function could be an ineffective quantity of milling balls and so a smaller impacts number for filling levels lower than 10%. On the other hand, an excessive interaction of the spheres (reduced velocity and kinetic energy, because of the numerous impacts or deviations) and a decrease of the number of collisions on the vial walls for filling degrees over 50% are also detrimental for the process. For a perfect enhancement of the energy transfer model, additional experiments are needed, to define clearly the situation at the lower and higher regions.

## References

1. Felderhoff, M.; Weidenthaler, C.; von Helmolt, R.; Eberle, U. Hydrogen storage: The remaining scientific and technological challenges. *Phys. Chem. Chem. Phys.* **2007**, *9*, 2643–2653. [[CrossRef](#)] [[PubMed](#)]
2. Ross, D.K. Hydrogen storage: The major technological barrier to the development of hydrogen fuel cell cars. *Vacuum* **2006**, *80*, 1084–1089. [[CrossRef](#)]
3. Bellosta von Colbe, J.; Ares, J.-R.; Barale, J.; Baricco, M.; Buckley, C.; Capurso, G.; Gallandat, N.; Grant, D.M.; Guzik, M.N.; Jacob, I.; et al. Application of hydrides in hydrogen storage and compression: Achievements, outlook and perspectives. *Int. J. Hydrogen Energy* **2019**, in press. [[CrossRef](#)]
4. Lide, D.R. *Handbook of Chemistry and Physics*; CRC Press: London, UK, 1994.
5. Varin, R.A.; Czujko, T.; Wronski, Z.S. *Nanomaterials for Solid State Hydrogen Storage*; Springer: New York, NY, USA, 2009.

6. Bossel, U.; Eliasson, B. Energy and the Hydrogen Economy, US DOE, EERE. Available online: [http://www.afdc.energy.gov/pdfs/hyd\\_economy\\_bossel\\_eliasson.pdf](http://www.afdc.energy.gov/pdfs/hyd_economy_bossel_eliasson.pdf) (accessed on 15 February 2019).
7. Von Helmolt, R.; Eberle, U. Fuel cell vehicles: Status 2007. *J. Power Sources* **2007**, *165*, 833–843. [[CrossRef](#)]
8. Jepsen, J.; Bellosta von Colbe, J.M.; Klassen, T.; Dornheim, M. Economic potential of complex hydrides compared to conventional hydrogen storage systems. *Int. J. Hydrogen Energy* **2012**, *37*, 4204–4214. [[CrossRef](#)]
9. Crivello, J.C.; Dam, B.; Denys, R.V.; Dornheim, M.; Grant, D.M.; Huot, J.; Jensen, T.R.; de Jongh, P.; Latroche, M.; Milanese, C.; et al. Review of magnesium hydride-based materials: Development and optimisation. *Appl. Phys. A* **2016**, *122*, 97. [[CrossRef](#)]
10. Yartys, V.A.; Lototskyy, M.V.; Akiba, E.; Albert, R.; Antonov, V.E.; Ares, J.R.; Baricco, M.; Bourgeois, N.; Buckley, C.E.; Bellosta von Colbe, J.M.; et al. Magnesium based materials for hydrogen based energy storage: Past, present and future. *Int. J. Hydrogen Energy* **2019**, in press. [[CrossRef](#)]
11. Milanese, C.; Jensen, T.R.; Hauback, B.C.; Pistidda, C.; Dornheim, M.; Yang, H.; Lombardo, L.; Zuetzel, A.; Filinchuk, Y.; Ngene, P.; et al. Complex hydrides for energy storage. *Int. J. Hydrogen Energy* **2019**, *44*, 7860–7874. [[CrossRef](#)]
12. Puzkiel, J.; Garroni, S.; Milanese, C.; Gennari, F.; Klassen, T.; Dornheim, M.; Pistidda, C. Tetrahydroborates: Development and Potential as Hydrogen Storage Medium. *Inorganics* **2017**, *5*, 74. [[CrossRef](#)]
13. Milanese, C.; Garroni, S.; Gennari, F.; Marini, A.; Klassen, T.; Dornheim, M.; Pistidda, C. Solid State Hydrogen Storage in Alanates and Alanate-Based Compounds: A Review. *Metals* **2018**, *8*, 567. [[CrossRef](#)]
14. Garroni, S.; Santoru, A.; Cao, H.; Dornheim, M.; Klassen, T.; Milanese, C.; Gennari, F.; Pistidda, C. Recent Progress and New Perspectives on Metal Amide and Imide Systems for Solid-State Hydrogen Storage. *Energies* **2018**, *11*, 1027. [[CrossRef](#)]
15. Barkhordarian, G.; Klassen, T.; Bormann, R. Fast hydrogen sorption kinetics of nanocrystalline Mg using Nb<sub>2</sub>O<sub>5</sub> as catalyst. *Scr. Mater.* **2003**, *49*, 213–217. [[CrossRef](#)]
16. Bösenberg, U.; Kim, J.W.; Goslar, D.; Eigen, N.; Jensen, T.R.; von Colbe, J.M.B.; Zhou, Y.; Dahms, M.; Kim, D.H.; Günther, R.; et al. Role of additives in LiBH<sub>4</sub>-MgH<sub>2</sub> reactive hydride composites for sorption kinetics. *Acta Mater.* **2010**, *58*, 3381–3389. [[CrossRef](#)]
17. Pighin, S.A.; Capurso, G.; Lo Russo, S.; Peretti, H.A. Hydrogen sorption kinetics of magnesium hydride enhanced by the addition of Zr<sub>8</sub>Ni<sub>21</sub> alloy. *J. Alloys Compd.* **2012**, *530*, 111–115. [[CrossRef](#)]
18. Suryanarayana, C. Mechanical alloying and milling. *Prog. Mater. Sci.* **2001**, *46*, 1–184. [[CrossRef](#)]
19. Garroni, S.; Pistidda, C.; Brunelli, M.; Vaughan, G.B.M.; Surinach, S.; Baro, M.D. Hydrogen desorption mechanism of 2NaBH<sub>4</sub> + MgH<sub>2</sub> composite prepared by high-energy ball milling. *Scr. Mater.* **2009**, *60*, 1129–1132. [[CrossRef](#)]
20. Huot, J.; Ravnsbæk, D.B.; Zhang, J.; Cuevas, F.; Latroche, M.; Jensen, T.R. Mechanochemical synthesis of hydrogen storage materials. *Prog. Mater. Sci.* **2013**, *58*, 30–75. [[CrossRef](#)]
21. Goslawit-Utke, R.; Thiangviriyia, S.; Javadian, P.; Laipple, D.; Pistidda, C.; Bergemann, N.; Horstmann, C.; Jensen, T.R.; Klassen, T.; Dornheim, M. Effective nanoconfinement of 2LiBH<sub>4</sub>-MgH<sub>2</sub> via simply MgH<sub>2</sub> premilling for reversible hydrogen storages. *Int. J. Hydrogen Energy* **2014**, *39*, 15614–15626. [[CrossRef](#)]
22. Capurso, G.; Agresti, F.; Crociani, L.; Rossetto, G.; Schiavo, B.; Maddalena, A.; Lo Russo, S.; Principi, G. Nanoconfined mixed Li and Mg borohydrides as materials for solid state hydrogen storage. *Int. J. Hydrogen Energy* **2012**, *37*, 10768–10773. [[CrossRef](#)]
23. Comănescu, C.; Capurso, G.; Maddalena, A. Nanoconfinement in activated mesoporous carbon of calcium borohydride for improved reversible hydrogen storage. *Nanotechnology* **2012**, *23*, 385401. [[CrossRef](#)] [[PubMed](#)]
24. Dornheim, M.; Doppiu, S.; Barkhordarian, G.; Boesenberg, U.; Klassen, T.; Gutfleisch, O.; Bormann, R. Hydrogen storage in magnesium-based hydrides and hydride composites. *Scr. Mater.* **2007**, *56*, 841–846. [[CrossRef](#)]
25. Westerwaal, R.J.; Haije, W.G. Evaluation solid-state hydrogen storage systems. *ECN Hydrog. Clean Foss. Fuels* **2008**, *3*, 19–21.
26. Barkhordarian, G.; Klassen, T.; Dornheim, M.; Bormann, R. Unexpected kinetic effect of MgB<sub>2</sub> in reactive hydride composites containing complex borohydrides. *J. Alloys Compd.* **2007**, *440*, L18–L21. [[CrossRef](#)]
27. Vajo, J.J.; Skeith, S.L.; Mertens, F. Reversible Storage of Hydrogen in Destabilized LiBH<sub>4</sub>. *J. Phys. Chem. B* **2005**, *109*, 3719–3722. [[CrossRef](#)] [[PubMed](#)]

28. Züttel, A.; Wenger, P.; Rentsch, S.; Sudan, P.; Mauron, P.; Emmenegger, C. LiBH<sub>4</sub> a new hydrogen storage material. *J. Power Sources* **2003**, *118*, 1–7. [[CrossRef](#)]
29. Jepsen, J.; Milanese, C.; Puszkiel, J.; Girella, A.; Schiavo, B.; Lozano, A.G.; Capurso, G.; Bellosta von Colbe, J.M.; Marini, A.; Kabelac, S.; et al. Fundamental Material Properties of the 2LiBH<sub>4</sub>-MgH<sub>2</sub> Reactive Hydride Composite for Hydrogen Storage: (I) Thermodynamic and Heat Transfer Properties. *Energies* **2018**, *11*, 1081. [[CrossRef](#)]
30. Jepsen, J.; Milanese, C.; Puszkiel, J.; Girella, A.; Schiavo, B.; Lozano, A.G.; Capurso, G.; Bellosta von Colbe, J.M.; Marini, A.; Kabelac, S.; et al. Fundamental Material Properties of the 2LiBH<sub>4</sub>-MgH<sub>2</sub> Reactive Hydride Composite for Hydrogen Storage: (II) Kinetic Properties. *Energies* **2018**, *11*, 1170. [[CrossRef](#)]
31. Puszkiel, J.A.; Castro Riglos, M.V.; Karimi, F.; Santoru, A.; Pistidda, C.; Klassen, T.; Bellosta von Colbe, J.M.; Dornheim, M. Changing the dehydrogenation pathway of LiBH<sub>4</sub>-MgH<sub>2</sub> via nanosized lithiated TiO<sub>2</sub>. *Phys. Chem. Chem. Phys.* **2017**, *19*, 7455–7460. [[CrossRef](#)] [[PubMed](#)]
32. Karimi, F.; Riglos, M.V.C.; Santoru, A.; Hoell, A.; Raghuwanshi, V.S.; Milanese, C.; Bergemann, N.; Pistidda, C.; Nolis, P.; Baro, M.D.; et al. In Situ Formation of TiB<sub>2</sub> Nanoparticles for Enhanced Dehydrogenation/Hydrogenation Reaction Kinetics of LiBH<sub>4</sub>-MgH<sub>2</sub> as a Reversible Solid-State Hydrogen Storage Composite System. *J. Phys. Chem. C* **2018**, *122*, 11671–11681. [[CrossRef](#)]
33. Le, T.-T.; Pistidda, C.; Puszkiel, J.; Castro Riglos, M.V.; Karimi, F.; Skibsted, J.; GharibDoust, S.P.; Richter, B.; Emmeler, T.; Milanese, C.; et al. Design of a Nanometric AlTi Additive for MgB<sub>2</sub>-Based Reactive Hydride Composites with Superior Kinetic Properties. *J. Phys. Chem. C* **2018**, *122*, 7642–7655. [[CrossRef](#)]
34. Santos, F.A.; Ramos, A.S.; Santos, C. d.; Suyuki, P.A.; Rodrigues Júnior, D. Efficiency Evaluation of ZrB<sub>2</sub> Incorporation in the MgB<sub>2</sub> Matrix Phase Using High-Energy Milling. *Mater. Sci. Forum* **2010**, *660–661*, 82–87. [[CrossRef](#)]
35. Pitt, M.P.; Paskevicius, M.; Webb, C.J.; Sheppard, D.A.; Buckley, C.E.; Gray, E.M. The synthesis of nanoscopic Ti based alloys and their effects on the MgH<sub>2</sub> system compared with the MgH<sub>2</sub> + 0.01Nb<sub>2</sub>O<sub>5</sub> benchmark. *Int. J. Hydrogen Energy* **2012**, *37*, 4227–4237. [[CrossRef](#)]
36. Burgio, N.; Iasonna, A.; Magini, M.; Martelli, S.; Padella, F. Mechanical alloying of the Fe–Zr system. Correlation between input energy and end products. *Il Nuovo Cimento D* **1991**, *13*, 459–476. [[CrossRef](#)]
37. Busch, N. *Optimierung des Herstellungsprozesses und der Zusammensetzung von Wasserstoffspeichermaterialien*; Fachhochschule Lübeck: Lübeck, Germany, 2012.
38. Werner, T. *Verbesserung der Wasserstoffspeichereigenschaften Eines Reaktiven Hydridkomposits durch Optimierung des Herstellungsprozesses*; Hochschule für Angewandte Wissenschaften Hamburg: Hamburg, Germany, 2013.
39. Pinkerton, F.E.; Meyer, M.S.; Meisner, G.P.; Balogh, M.P.; Vajo, J.J. Phase Boundaries and Reversibility of LiBH<sub>4</sub>/MgH<sub>2</sub> Hydrogen Storage Material. *J. Phys. Chem. C* **2007**, *111*, 12881–12885. [[CrossRef](#)]
40. Bösenberg, U. *LiBH<sub>4</sub>-MgH<sub>2</sub> Composites for Hydrogen Storage*; Technische Universität Hamburg-Harburg: Hamburg, Germany, 2009.
41. Scherrer, P. Bestimmung der Größe und der inneren Struktur von Kolloidteilchen mittels Röntgenstrahlen. *Nachrichten von der Gesellschaft der Wissenschaften zu Göttingen, Mathematisch-Physikalische Klasse* **1918**, *1918*, 98–100. [[CrossRef](#)]
42. Pretzel, F.E.; Rupert, G.N.; Mader, C.L.; Storms, E.K.; Gritton, G.V.; Rushing, C.C. Properties of lithium hydride I. Single crystals. *J. Phys. Chem. Solids* **1960**, *16*, 10–20. [[CrossRef](#)]
43. MatWeb. Available online: <http://www.matweb.com> (accessed on 15 September 2018).
44. Puszkiel, J.A.; Gennari, F.C.; Larochette, P.A.; Ramallo-López, J.M.; Vainio, U.; Karimi, F.; Pranzas, P.K.; Troiani, H.; Pistidda, C.; Jepsen, J.; et al. Effect of Fe additive on the hydrogenation-dehydrogenation properties of 2LiH + MgB<sub>2</sub>/2LiBH<sub>4</sub> + MgH<sub>2</sub> system. *J. Power Sources* **2015**, *284*, 606–616. [[CrossRef](#)]
45. Busch, N.; Jepsen, J.; Pistidda, C.; Puszkiel, J.A.; Karimi, F.; Milanese, C.; Tolkiehn, M.; Chaudhary, A.-L.; Klassen, T.; Dornheim, M. Influence of milling parameters on the sorption properties of the LiH-MgB<sub>2</sub> system doped with TiCl<sub>3</sub>. *J. Alloys Compd.* **2015**, *645*, S299–S303. [[CrossRef](#)]
46. Deprez, E.; MunPoz-Mairquez, M.A.; Roldain, M.A.; Prestipino, C.; Palomares, F.J.; Minella, C.B.; Bösenberg, U.; Dornheim, M.; Bormann, R.; Fernández, A. Oxidation State and Local Structure of Ti-Based Additives in the Reactive Hydride Composite 2LiBH<sub>4</sub> + MgH<sub>2</sub>. *J. Phys. Chem. C* **2010**, *114*, 3309–3317. [[CrossRef](#)]

47. Deprez, E.; Justo, A.; Rojas, T.C.; López-Cartés, C.; Bonatto Minella, C.; Bösenberg, U.; Dornheim, M.; Bormann, R.; Fernández, A. Microstructural study of the  $\text{LiBH}_4\text{-MgH}_2$  reactive hydride composite with and without Ti-isopropoxide additive. *Acta Mater.* **2010**, *58*, 5683–5694. [[CrossRef](#)]
48. Wang, Y.; Wang, H.Y.; Yang, Y.F.; Jiang, Q.C. Solidification behavior of cast  $\text{TiB}_2$  particulate reinforced Mg composites. *Mater. Sci. Eng. A* **2008**, *478*, 9–15. [[CrossRef](#)]
49. Qiu, D.; Zhang, M.X.; Fu, H.M.; Kelly, P.M.; Taylor, J.A. Crystallography of recently developed grain refiners for Mg–Al alloys. *Philos. Mag. Lett.* **2007**, *87*, 505–514. [[CrossRef](#)]
50. Jepsen, J.; Milanese, C.; Girella, A.; Lozano, G.A.; Pistidda, C.; Bellosta von Colbe, J.M.; Marini, A.; Klassen, T.; Dornheim, M. Compaction pressure influence on material properties and sorption behaviour of  $\text{LiBH}_4\text{-MgH}_2$  composite. *Int. J. Hydrogen Energy* **2013**, *38*, 8357–8366. [[CrossRef](#)]
51. De Rango, P.; Chaise, A.; Charbonnier, J.; Fruchart, D.; Jehan, M.; Marty, P.; Miraglia, S.; Rivoirard, S.; Skryabina, N. Nanostructured magnesium hydride for pilot tank development. *J. Alloys Compd.* **2007**, *446–447*, 52–57. [[CrossRef](#)]
52. Çakmak, G.; Öztürk, T. Milling of magnesium powders without additives. *Powder Technol.* **2013**, *237*, 484–488. [[CrossRef](#)]



© 2019 by the authors. Licensee MDPI, Basel, Switzerland. This article is an open access article distributed under the terms and conditions of the Creative Commons Attribution (CC BY) license (<http://creativecommons.org/licenses/by/4.0/>).